

Contents lists available at ScienceDirect

Journal of Energy Chemistry

JOURNAL OF ENERGY CHEMISTRY

http://www.journals.elsevier.com/ iournal-of-energy-chemistry

journal homepage: www.elsevier.com/locate/jechem

Electrocatalytic production of glycolic acid via oxalic acid reduction on titania debris supported on a TiO₂ nanotube array

Francesco Pio Abramo ^a, Federica De Luca ^a, Rosalba Passalacqua ^a, Gabriele Centi ^a, Gianfranco Giorgianni ^b, Siglinda Perathoner ^a, Salvatore Abate ^{a,*}

ARTICLE INFO

Article history: Received 4 October 2021 Revised 15 December 2021 Accepted 17 December 2021 Available online 28 December 2021

Keywords: Oxalic acid TiO₂ nanotubes Glyoxylic acid Glycolic acid Electrocatalysis

ABSTRACT

Electrodes prepared by anodic oxidation of Ti foils are robust and not toxic materials for the electrocatalytic reduction of oxalic acid to glycolic acid, allowing the development of a renewable energy-driven process for producing an alcoholic compound from an organic acid at low potential and room temperature. Coupled with the electrochemical synthesis of the oxalic acid from CO_2 , this process represents a new green and low-carbon path to produce added value chemicals from CO_2 . Various electrodes prepared by anodic oxidation of Ti foils were investigated. They were characterized by the presence of a TiO_2 nanotube array together with the presence of small patches, debris, or TiO_2 nanoparticles. The concentration of oxygen vacancies, the amount of Ti^{3+} measured by X-ray photoelectron spectroscopy (XPS) and the intensity of the anodic peak measured by cyclic voltammetry, were positively correlated with the achieved oxalic acid conversion and glycolic acid yield. The analysis of the results indicates the presence of small amorphous TiO_2 nanoparticles (or surface patches or debris) interacting with TiO_2 nanotubes, the sites responsible for the conversion of oxalic acid and glycolic acid yield. By varying this structural characteristic of the electrodes, it is possible to tune the glycolic acid to glyoxylic acid relative ratio. A best cumulative Faradaic efficiency (FE) of about 84% with FE to glycolic acid around 60% and oxalic conversion about 30% was observed.

© 2021 Science Press and Dalian Institute of Chemical Physics, Chinese Academy of Sciences. Published by ELSEVIER B.V. and Science Press. All rights reserved.

1. Introduction

The production of high-value chemicals by electrocatalytic reduction of CO₂ is one of the current challenges in energy chemistry to foster a fossil-free chemical industry based on renewable energy sources [1–4]. While C1 products obtained by CO₂ reduction (CO, CH₃OH, formic acid) have a relatively low commercial value, they enable the production of C2 and C3 (multicarbon) fuels, and chemicals open a range of novel and exciting possibilities from the industrial perspective. Thus C1 products can be considered the gate to deploy the electrocatalytic processes of CO₂ utilization [5–10]. However, the range of products obtainable by direct electrocatalytic reduction of CO₂ is relatively limited (primarily ethylene, ethanol, and acetic acid/acetate). Alternatives to the direct reduction, a multistep path with the initial production of oxalic acid (OX, directly or indirectly via formic acid as intermediate) and then the electrocatalytic reduction of OX [5] along the paths drawn in

Scheme 1 creates a new value chain [5]. Between the possible products, glyoxylic acid (GO) and glycolic acid (GC), obtainable from OX in a sequence of concerted two proton-electron transfer, are of special interest being high added-value chemicals, with an interesting potential market [5].

GC is used in several industries as an α -hydroxy acid: (i) in the textile industry as a whitener and tanning agent, (ii) in the food industry as a flavouring, (iii) in the polymers industry as a monomer for the synthesis of polyglycolic acid (PGA), a biodegradable and thermoplastic polymer, or of poly(lactic-co-glycolic) acid (PLGA), a biodegradable and biocompatible copolymer employed in the fabrication of therapeutic devices [11]. GO is used to produce pharmaceuticals, agrochemicals, and various food, personal care, and cosmetics components. GO and GC markets are forecast to reach together over one billion US\$ by 2025. In addition, the market value of GO and GC is currently around 4000 and 2000 € ton $^{-1}$, respectively, thus up to 2–3 times larger than the average for petrochemical intermediates. They are produced industrially with complex multistep processes. More specifically, GC is currently produced either by the hydrative carbonylation of formaldehyde

a Department of ChiBioFarAM (Industrial Chemistry), University of Messina, ERIC aisbl and INSTM/CASPE, V.le F. Stagno d'Alcontres 31, Messina 98166, Italy

b University of Calabria, Department of Environmental Engineering, Laboratory of Industrial Chemistry and Catalysis Via P. Bucci, 87036 Rende, CS, Italy

^{*} Corresponding author.

E-mail address: abates@unime.it (S. Abate).

Scheme 1. Simplified reaction network in the electrocatalytic conversion of CO_2 to C2 high added value chemicals.

under very harsh conditions or by chlorination of acetic acid followed by hydrolysis of the resulting chloroacetic acid in the presence of sodium hydroxide. GO is produced by selective catalytic oxidation of GC, and for this reason, its commercial value is about twice that of GC. Thus, producing them from CO₂ by an electrocatalysis route could combine (i) process intensification, (ii) recycling of waste CO2 and (iii) introduction of renewables in the production chain. The electrocatalytic path from OX combines (i) a potential cost reduction, (ii) a reduced carbon footprint, (iii) a process simplification (reduction and integration of steps), (iv) the use of environmentally more friendly industrial operations, (v) the substitution of fossil fuels as raw material and (vi) the use of renewable energy sources for the process. In other words, it is a good example of innovation towards a sustainable production. In addition, the current market for GO is strongly dependent on the cost and availability of GC being the raw material for GO. Producing GO from OX can thus decouple the two processes, although the electrocatalytic route has the great inherent advantage of allowing to produce both chemicals in the same equipment, and thus introduce also flexibility to better adapt to variable markets.

From an industrial perspective, the electrocatalytic route from OX as intermediate is thus quite attractive and would be relevant to determine the conditions to maximize the production of GO or GC. The use of bio-based raw materials and catalytic or enzymatic processes represents an alternative possibility, but still, the processes are at the lab-scale development [12]. Note also that as remarked in Scheme 1, the route can be extended to produce in a sustainable process also other chemicals such as tartaric acid [13], besides to a range of valuable derivatives of GO and GC, not shown in Scheme 1 for conciseness.

Earlier studies on the electrocatalytic reduction of OX use a lead cathode [14,15], but with the severe drawbacks of deactivation and harmful effects of Pb for the environment and humans [16]. To overcome these issues, alternative cathode materials more sustainable and with a better selectivity to GC or GO should be developed. However, literature data on this aspect are limited. The use of TiO₂ to replace the lead cathode was proposed by Masaaki et al. [17]. They used a porous anatase TiO2 directly grown on a Ti mesh, and Ti felt as a cathode but coupled with a costly IrO₂-based anode. GC was obtained with 50% selectivity, while GO formed in minor amounts. Conversion of OX was also low (<15%) at the optimal applied voltage of 2.4 V. In addition, the catalyst was deactivated within one hour. These results are in contrast with an earlier finding by Zhao et al. [18] that used a roughened TiO₂ film electrode prepared by anodic oxidation. They evaluated the behavior of these electrodes in a batch-type undivided electrochemical cell, applying high voltages (2.9–3.4 V). Even with the differences in conditions and type of electrocatalytic reactor, they observed GO rather than GC formation, with a maximum yield of about 57% after 8 h at 3.3 V. The yield dropped significantly when a Ti polished electrode

rather than the roughened TiO₂ film electrode was used. The latter suggests that titania specific characteristics likely determine the electrocatalytic behavior in OX reduction. This indication is supported by De Luca et al. [19], showing that a composite electrode based on graphite-C₃N₄ decorating TiO₂ nanotubes is able to give a GC selectivity up to 76%, while pristine TiO₂ nanotubes are less selective (about 34%). The effect seems associated to the modification of the electronic structure of TiO₂ induced by the heterojunction with g-C₃N₄. Thus, nanostructured TiO₂ appears as a promising material to develop cathodes for the OX electrocatalytic reduction. However, quite limited data are available in the literature, while indications about the specific role of titania and how to optimize the electrocatalytic performances are contrasting.

Here we thus aim to study the electroreduction of OX by using as cathode a ${\rm TiO_2}$ film of well-ordered and vertically aligned ${\rm TiO_2}$ nanotubes (grown by anodic oxidation on a Ti plate acting as electrode conductive substrate; ${\rm TiO_2NT/Ti}$) [20–25]. The advantage of this nanostructure is the good accessibility to the inner part of the nanotube due to the vertical-aligned structure and internal size in the 50–100 nm range. Thus, a high active (accessible) surface (a three-dimensional (3D)-like electrode) can be obtained with respect to a ${\rm TiO_2}$ layer obtained by compact ${\rm TiO_2}$ nanoparticles. In addition, due to this nanostructure, an enhanced electrical conductivity is induced with respect to a thin titania film of equivalent thickness [26]. Finally, the electrode results robust and easily scalable for industrial applications.

However, the specific characteristics of the electrode [27–29] depend largely on the details of the preparation method. We have thus selected here for this study TiO₂NT/Ti electrodes prepared by different procedures (as described later), in order to tailor the characteristics of these electrodes. They were compared as benchmarking with TiO2 (unordered) nanotubes prepared by hydrothermal synthesis and then deposited over the Ti substrate [30,31]. By comparing the physico-chemical and reactivity characteristics of TiO₂-NT/Ti electrodes, with respect to benchmarking electrodes, it is thus possible to understand better the nature of the titania species involved in the electroreduction of OX and the factors allowing to tune the performances and selectivity, operating at the same time at significantly lower applied potentials than what reported in earlier studies (around -1.1 vs. Ag/AgCl), an important aspect in terms of results exploitability. Nanostructured TiO₂ electrodes find application in a range of energy uses, from dye-sensitized solar cell (DSSC) to batteries, besides that as robust electrodes for electrochemical applications [32–36]. The study can be thus relevant for the entire field of titania-based electrodes as advanced energy materials.

The work here is focused, for clarity, only on the electrocatalytic OX reduction to GO and GC, but the other aspects outlined in Scheme 1, in particular, the direct and indirect paths of OX formation from CO₂, are also investigated as part of the European project OCEAN (Oxalic acid from CO₂ using electrochemistry at demonstration scale, project 767798) aimed to develop at a demo scale a new value chain in producing C2 chemicals from CO₂.

2. Experimental

2.1. Preparation of the electrocatalysts

TiO₂ nanotubes were synthesized by controlled anodic oxidation (AO) of titanium foils (Alfa Aesar) and of a commercial P25 Degussa TiO₂ under hydrothermal conditions. The AO method leads to a self-ordered array (ordered hexagonal closely packed) of vertically-aligned TiO₂ nanotubes grown directly on the Ti foil acting as an electron-conductive substrate for the electrode (oTiO₂-NT/Ti). Changes in the procedure lead to different electrodes, as

described in section 2.1.1. The hydrothermal method leads to a powder formed by not-ordered overlapping TiO_2 nanotubes. This powder is then deposited over the Ti foil to prepare the electrode ($uTiO_2NT/Ti$).

2.1.1. Anodic oxidation of Ti foils

Ti foils (Alfa Aesar, diameter 35 mm, thickness 0.025 mm, purity 99.96 %) were used (a) as received or (b) after pre-calcination at 450 °C for 30 min. Before the AO procedure, all the Ti foils were washed sequentially for 10 min in (i) distilled water, (ii) acetone, and (iii) isopropyl alcohol by using an ultrasonic bath. AO of washed Ti foils was carried out at room temperature for 1 h in a two-electrode configuration cell equipped with a glassy carbon cathode, employing a constant applied potential of 50 V, using an aged electrolyte solution of NH₄F (0.3 wt% - Sigma-Aldrich, \geq 98%), deionized water (2 wt%), and ethylene glycol (98wt % - Sigma-Aldrich, 99.8%). The obtained TiO₂NT/Ti was (a) rinsed by deionized water to remove the residual electrolyte, (b) dried overnight, and (c) calcined at 450 °C for 3 h with a temperature ramp of 2 °C min $^{-1}$.

By using the above-reported procedure, a set of three catalysts was prepared (Table 1). The TiNT and TiNT-A electrodes were prepared by varying the aging time between 60 and 240 min. The electrode aging time is the electrolyte–electrode contact time before applying the 50 V potential. In both cases, only cleaned Ti-foils were used. In the TiNT-T electrode case, the Ti foil was instead pre-calcined at 450 °C (30 min). The other aspects of the procedure remained unchanged.

2.1.2. Hydrothermal catalyst synthesis

0.46 g of Degussa P25 $\rm TiO_2$ (purity 99.9%, 85% Rutile and 25% Anatase, surface area 50 m² g⁻¹, pore volume 0.11 cm³ g⁻¹, density 4.26 g cm⁻³) were dispersed in 65 mL of 10 M NaOH solution by using an ultrasonic bath for 15 min. The resulting suspension was hydrothermally treated in a Teflon-lined, stirred autoclave at 130 °C for 24 h with a stirring rate of 600 r min⁻¹. The hydrothermally treated sample was vacuum filtered and washed till neutral pH was reached. Then, it was protonated at room temperature in 0.1 M HCl under stirring (600 r min⁻¹) for 1 h. The protonated sample was rinsed with distilled water till neutral pH, dried at 80 °C overnight, and grounded. The resulting powder was dispersed in methanol (10 mg mL⁻¹) and deposited on a Ti foil using an airbrush (ABEST TJ-180 K) to reach a theoretical TiO₂ loading of 1.5 mg cm⁻².

The as-prepared sample was dried at 80 °C overnight and, finally, calcined at 450 °C for 3 h (2 °C min $^{-1}$), obtaining an experimental TiO $_2$ loading of 0.7 mg cm $^{-2}$. The prepared catalyst is referenced as TiNT-HS hereinafter (Table 1).

2.2. Experimental apparatus and electrodes testing procedure

The electrodes indicated in Table 1 were tested as cathodes in the electrocatalytic reduction of OX using the apparatus presented schematically in the Supplementary Info (Fig. S1a). The electrocatalytic cell uses a proton-exchange membrane (Nafion® 115) at the interface between the anodic (1) and cathodic (2) compartments and two external reservoirs for catholyte and anolyte. A 0.03 M

Table 1Overview of the samples prepared and the acronym used.

Name	Pre-treatment	Aging time (minutes)	Method
TiNT TiNT-A	None None	60 240	Anodic oxidation Anodic Oxidation
TiNT-T	Calcination	60	Anodic Oxidation
TiNT-HS	None	-	Hydrothermal synthesis

OX solution (pH = 2) containing a 0.2 M Na_2SO_4 solution was used in the cathodic compartment. In the anodic compartment, a 0.2 M Na_2SO_4 electrolyte solution was used. The pH of the anodic electrolyte solution was adjusted by adding controlled amounts of a 1 M H_2SO_4 solution until obtaining the same pH of the catholyte. A peristaltic pump was used to circulate the electrolytes. The volume of the electrolytic solution (cathode + external tank + tubes) was 35 ml, while, in the electrocatalytic cell, the net electrolyte volume was 7 mL.

The amperometric detection experiments (AD) were performed at constant applied potential, in the range between -1.1 to -1.3 V at 25 °C, and monitoring the current density by an Amel potentiostat/galvanostat (Model 2551) for 2 h. All potentials were measured with respect to Ag/AgCl, while $\rm H_2$ was generated in situ by water co-electrolysis. The surface electrode was 5.7 cm². A Metrohm 940 Professional ionic chromatograph, equipped with a column for organic acids, was used to determine the concentration of the products formed at the cathode side of the electrocatalytic cell (a representative chromatogram is reported in Fig. S1b).

The following equations are used to express the electrocatalytic reactivity:

Faradaic efficiency (%) =
$$\frac{m_{\text{product}} \times n \times F}{Q} \times 100$$
,

where $m_{\rm product}$ represents the moles of the reduction products; n represents the number of electrons required for the formation of GO and GC from OX (n = 2 and 4 for the formation of GO and GC, respectively); F is the Faradaic constant (96485 C mol⁻¹ of electrons); Q is the total charge in Coulombs passed across the electrode during the electrolysis.

OX conversion in electro-reduction experiments was defined using the following equation:

$$\label{eq:ox_conversion} OX \ conversion \ (\%) \ = \frac{[OX]_i - [OX]_t}{[OX]_i} \times 100,$$

where $[OX]_i$ is the initial OX concentration and $[OX]_t$ is the OX concentration after 2 h of reaction time.

The yield (Y) of the product is calculated

$$\label{eq:Yield_to_moduct} \mbox{Yield to } m_{product}(\%) \ = \frac{[M]_t}{[OX]_i} \times 100,$$

where $[M]_t$ is the concentration of $m_{product}$ after 2 h of reaction time. [OX], [GO], and [GC] are the molar concentrations of OX, GO, and GC, respectively.

2.3. Characterization methods

An XL-30 field emission scanning electron microscope (FEI/Philips), equipped with a high-brightness field emission gun (FEG) working at 3 kV, was used to investigate the nanostructure of the electrodes prepared.

PHI VersaProbe II (Physical Electronics), equipped with an Al K_{α} (1486.6 eV) X-ray source, measured the X-ray photoelectron spectroscopy (XPS) spectra. The survey spectra were recorded with an analyzer energy path of 117 eV, while the C 1s, O 1s, and Ti 2p core levels were measured at 23.5 eV. The X-ray beam size was 100 microns at 25 W. A charge neutralization procedure was performed by simultaneously irradiating samples using a low-energy electron beam and an ion beam before measuring the spectra. The position of the XPS peaks was referenced to graphite carbon (284.8 eV). XPS peaks were deconvoluted using the Multipack Data Reduction Software (ULVAC-PHI, Inc), employing a Shirley background curve.

A potentiostat/galvanostat (Amel 2551) measured the cyclic voltammetry (CV) curves of the prepared electrocatalysts, both in the presence and in the absence (blank) of OX as substrate. All

the samples were measured from 0 to -2 V potential (with respect to Ag/AgCl electrode) and a scan rate of 50 mV s⁻¹, using the apparatus reported in Fig. S2. Before CV measurements, the electrochemical cell was purged with Argon (20 mL min⁻¹) for 30 min. The CV curves are presented using the IUPAC convention.

The surface area of self-supported thin films was determined by the physical adsorption of N_2 onto the surface of the samples at liquid nitrogen temperatures by using an Autosorb IQ3 sorption analyzer (Quantachrome) system.

3. Results

3.1. Characteristics of the samples prepared by anodic oxidation of Ti foils

3.1.1. Anodic oxidation curves

To illustrate the differences in the characteristics of the preparation of the three samples synthetized by anodic oxidation of Ti foils (see Table 1 for a summary), Fig. 1 reports the anodization curves of current measured versus anodization time.

TiNT and TiNT-A were prepared following the same anodization procedure but changing the aging time. TiNT-T electrode instead was prepared as TiNT sample, but the Ti-foil is pre-calcinated before the anodization procedure. These relatively minor differences induce, however, significant changes in the anodization process (Fig. 1). To better describe the differences, it is necessary to introduce shortly the mechanism of formation of the TiO₂ NTs.

The formation of TiO_2 NTs in the anodization process occurs through the simultaneous action of (a) the electrochemical oxidation of Ti to TiO_2 (eq. 1) and (b) the F⁻ driven chemical dissolution of TiO_2 (eq. 2), both induced by the electric field [37].

$$Ti + 2H_2O \rightarrow TiO_2 + 4H^+ + 4e^-,$$
 (1)

$$TiO_2 + 6F^- + 4H^+ \rightarrow [TiF_6]^{2-} + 2H_2O.$$
 (2)

The mechanism and description of the steps in the anodization curves is well established through the following mechanism [38,39]:

 Generation of a dense non-conductive oxide layer on Ti foils and pore nucleation: after applying the potential, there is a sudden decrease of the measured current due to the growth of the oxi-

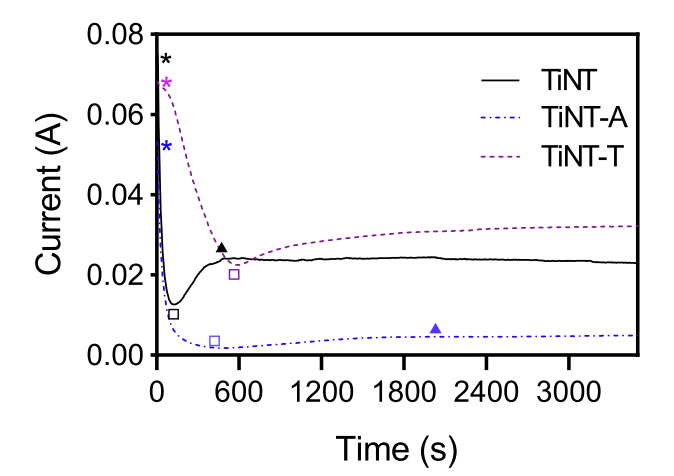


Fig. 1. Current versus time during the anodic oxidation (50 V, 1 h; *, \Box , \triangleq indicate for each curve, I_0 , I_{\min} and I_{\max} , respectively).

- dic layer. After that, the current decrease at a lower rate. The current rate change marks the beginning of pore nucleation till the minimum current is reached (I_{min}).
- 2. Pores generation: the current increase due to the dissolution of the oxide up to the maximum current ($I_{\rm max}$) is reached.
- 3. Nanotubes growth: the measured current slowly decreases due to the unbalance between the oxidation (eq. 1) and dissolution (eq. 2) steps.
- 4. Debris formation: nanotubes growth is stopped, the current remains stable or slowly decreases due to the formation of irregular oxide particles (debris) on the top surface of the nanotube ordered array.

The TiNT sample, prepared with cleaned Ti foil and an aging time of 60 min, shows an initial current (I_0) of 0.075 A, with a rapid decrease of the current in the first 120 s with a minimum (I_{\min}) and maximum current (I_{\max}) of about 0.0124 and 0.0241 A shown at 120 s (t_{\min}) and 480 s (t_{\max}), respectively. After 480 s, only a small drop in the current was measured up to the end of the anodization procedure (final current 0.0234 A).

After increasing the electrode aging time from 60 (Ti-NT) to 240 min (TiNT-A), I_0 decreased by 30% with respect to the TiNT sample. Although the slope shown by the initial decrease in the current was only slightly lower for both TiNT-A and TiNT samples, in the case of the TiNT-A sample, $I_{\rm min}$ and $I_{\rm max}$ (0.046 A) were significantly lower while, $t_{\rm min}$ and $t_{\rm max}$ increased up to 470 and 1800 s, respectively.

TiNT-T behavior is different. I_0 was 10% lower than TiNT, but current decreases upon potential application much less sharply, reaching t_{\min} after 570 s (I_{\min} of 0.022 A). Then, the current slowly increases up to the end of the test without showing a maximum current (I_{\max}).

The lower I_0 shown by the TiNT-A with respect to the TiNT sample was related to the depletion of F^- ions due to the increased aging time. In agreement, the decreased I_{\min} and I_{\max} and, as well, the increased t_{\min} and t_{\max} , indicate the formation of a dense oxidic layer with increased thickness (eq. 1), and decreased pore nucleation and nanotube growth rates (eq. 2). Thus, the formation of nanotubes is less effective in the TiNT-A sample.

In TiNT-T case, the initial less sharp decrease in the current derives from thin ${\rm TiO_2}$ film formed during pre-oxidation step, limiting thus the exposition of metallic Ti and affecting both the reactions reported in (eqs. 1 and 2). The presence of an oxide pre-layer, formed during the precalcination step, inhibits partially the formation of cracks/pits with exposed Ti, where the stronger electrical field induces the ${\rm TiO_2}$ NTs formation. The absence of a clear $I_{\rm max}$ delayed the pore nucleation step and nanotube growth (eq. 2), which is still active after 3500 s.

Thus, the different trends of the anodization curves for TiNT, TiNT-A, and TiNT-T electrodes can be well described based on literature indications [37–39]. However, what is relevant here is that the samples selected for this study can be well representative of different situations obtained in the formation of the ordered array of TiO_2 nanotubes and titania debris on it.

3.1.2. Scanning electron microscopy (SEM)

The SEM top-view micrographs of the electrodes prepared by anodic oxidation are reported in Fig. 2 (a–c for TiNT, TiNT-A, and TiNT-T, respectively). Also, the SEM micrograph of the sample of TiO_2 nanotubes prepared by hydrothermal treatment and deposited then on Ti foil (TiNT-HS) is reported for comparison (Fig. 2d).

Fig. 2(a) shows the surface of TiNT, evidencing the presence of the ordered array of vertically-aligned TiO_2 NTs partially covered on the surface by TiO_2 debris. The TiO_2 nanotubes are compact and dense with an inner diameter ranging from 50 to 100 nm and a wall thickness of about 15–20 nm. Fig. 2(b) shows the top

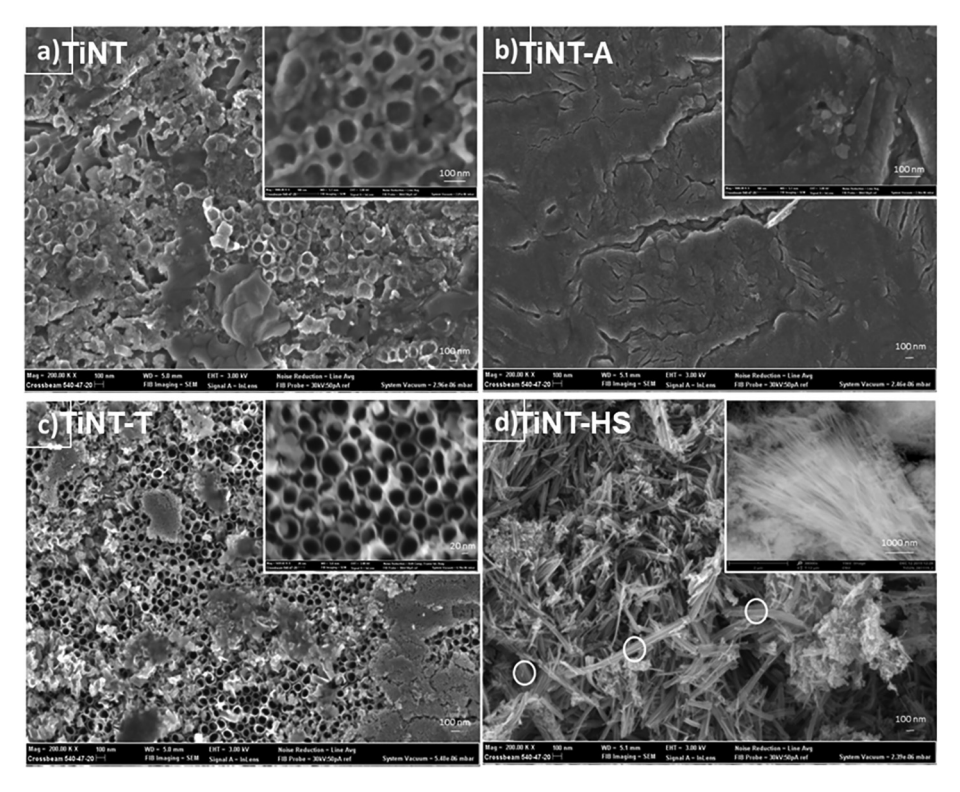


Fig. 2. SEM top-view images of the prepared electrodes. Insets show higher magnification micrographs.

view of the TiNT-A electrode, evidencing the presence of a surface compact oxide layer without the apparent presence of an undelaying TiO₂ NTs array. This is consistent with the anodization curve due to the depletion of F⁻ ions in the aged electrolyte solution [38,40]. Fig. 2(c) shows the top-view of the TiNT-T electrode, where the underlying TiO₂ NTs array is well evidenced but covered on the surface by large porous oxide patches, more compacts with respect to debris present in TiNT. In the TiNT-T case, with respect to TiNT, TiO₂ NTs show a more uniform inner diameter (ranging from 40 to 60 nm) and a thinner wall thickness (around 10 nm), but a slightly lower density of TiO₂ NTs packing. Fig. S2 in the Supplementary Info reports an additional view of the TiNT-T sample after cracking the layer to better reveal the presence of a highly ordered and aligned vertically array of TiO₂ NTs with homogeneous dimensions and a well-defined structure. The results are consistent with indications given by Macak et al. [41], reporting an improved ordering of the tubes by using pre-structured surfaces. In our case, the thermal pretreatment creates the initiation sites for TiO₂ NTs growth during the anodization process, leading to a more defined nanostructure with respect to TiNT, although the presence of large TiO₂ patches rather than debris as in TiNT is observed. The EDX analysis reported in Fig. S2a confirm the elemental composition based on a homogeneous TiO2 layer with negligible traces of F observed on both TiNT and TiNT-T samples.

The titania film thickness in all TiNTs samples ranges in the 0.7–0.8 μm range.

The SEM micrographs of the TiNT-HS sample (Fig. 2d) show the presence of nanosheets (white circles) and tubular nanostructures randomly oriented (see inset), in agreement with Moazeni et al. [42] also reporting similar indications. The packing of these TiO_2 nanosheets and nanotubes is less dense with respect to TiNT samples.

3.1.3. Cyclic voltammetry

In order to characterize the differences between these samples and the impact on redox behavior, the electrodes were studied by CV [43–46]. Fig. 3(a) shows the voltammograms measured in a 0.2 M Na_2SO_4 solution (blank solution) for all the investigated samples. A reversible reduction peak at -1.26 V was observed for all samples and related to the reduction of Ti^{4+} to Ti^{3+} according to eq. 3:

$$TiO_2 + H_2O + H^+ + e^- \leftrightarrow Ti(OH)_3.$$
 (3)

At -1.60 V starts the formation of gaseous hydrogen according to the eq. 4:

$$2H^+ + 2e^- \rightarrow H_2$$
. (4)

The negative current in this region is related to this reaction. The proton insertion-coupled electron transfer reaction occurs in parallel (eq. 5) [46]:

$$TiO_2 + xe^- + xH^+ \leftrightarrow Ti^{IV}_{1-x}Ti^{III}_x (O)_{1-x}(OH)_x.$$
 (5)

The decomposition of this product gives rise to the anodic peak around -1.5 V. For all the samples, an anodic peak in between -0.8 and -0.9 V is also observed and attributed to the oxidation of $\rm Ti^{3^+}$ to $\rm Ti^{4^+}$. The peak intensity follows the order TiNT-T > TiNT-HS > Ti NT > TiNT-A, suggesting the presence of a larger amount of $\rm Ti^{3^+}$ species in the TiNT-T sample. Quantification and correlation of these results with other characterization aspects will be discussed later.

In the presence of OX 0.03 M (Fig. 3b), the anodic peaks become much less intense due to the decreased oxidation of Ti³⁺ species, while the cathode current slightly increased.

The decreased intensity of such anodic peaks in OX solution suggests that the electrogenerated Ti³⁺ species reduces OX, in agreement with Zhao et al. [18], who observed similar behavior on a rough TiO₂ layer. In order to confirm this interpretation, a CV profile was performed on the TiNT sample by using a high concentration of OX (0.1 M), see Fig. S3 (Supplementary Info). A higher cathode current was observed in the latter case, while the oxida-

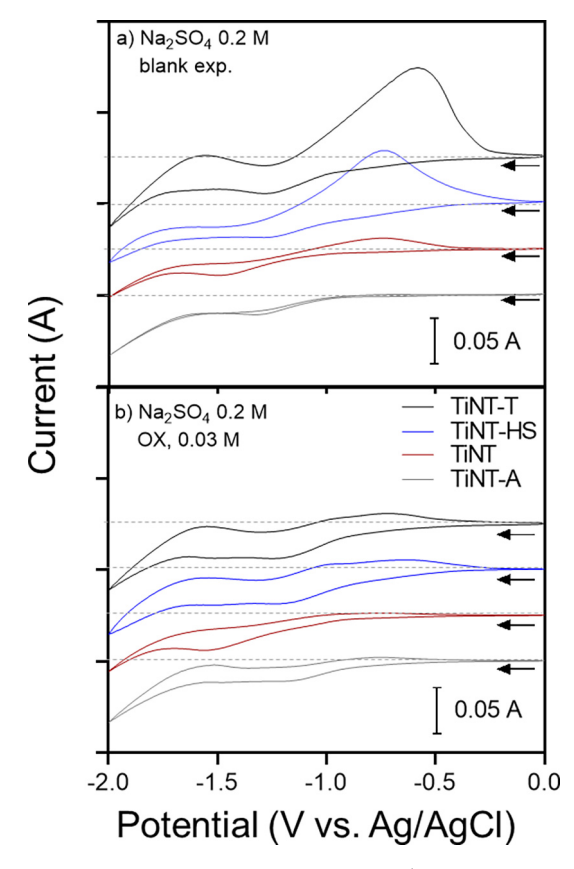


Fig. 3. CV, recorded with a scanning rate (ν) of 50 mV s⁻¹ in (a) Na₂SO₄ 0.2 M (blank experiment), and (b) adding an OX solution 0.03 M.

tion peak totally disappeared, confirming the electroreduction of OX by the electrons generated by the Ti³⁺/Ti⁴⁺ redox couple.

These results indicate that the nanoporous TiO₂ film electrode acts as a good heterogeneous redox catalytic electrode, and OX undergoes fast chemical electroreduction.

3.1.4. X-ray photoelectron spectroscopy

The surface characteristics of TiNT electrodes were investigated by photoelectron spectroscopy. The survey spectra (Fig. S4 in the Supplementary Info) indicate that TiO₂ nanotubes contain mainly Ti and O elements while no other impurities, except (as normal) the contamination by carbon (C 1s peak). Other survey spectra, not reported for conciseness, show similar features.

The high-resolution XPS spectra were measured for Ti 2p and O 1s. The Ti 2p core level spectra are reported in Fig. S5 (Supplementary Info) for all the samples investigated. Ti 2p spectra are deconvoluted in two peaks, the doublet Ti $2p_{3/2}$ at 458.50 ± 0.1 eV and Ti $2p_{1/2}$ at 464.04 ± 0.1 eV that are consistent with Ti⁴⁺ in TiO₂ lattice [47,48]. The shoulder peaks at 456.91 ± 0.1 eV and 462.45 ± 0.1 eV are assigned to Ti $2p_{3/2}$ and Ti $2p_{1/2}$ and correspond to Ti³⁺species Ti₂O₃ [49]. The Ti $2p_{1/2}$ -Ti $2p_{3/2}$ splitting energy was 5.54 eV.

All the high-resolution O 1s core level spectra, reported in Fig. 4, exhibit an asymmetric curve and a narrow shoulder, indicating the presence of a larger concentration of oxygen species in the near-surface region [50]. The O 1s spectrum of each sample was deconvolved into two asymmetrical peaks named O1 and O2v. The intense O1 peak, shown at 529.81 \pm 0.2 eV, was attributed to the oxygen contained in the TiO₂ crystal lattice, while the O2v peak at 531.32 \pm 0.2 eV was attributed to the oxygen bound to Ti³⁺ species within Ti₂O₃, associated with a surface oxygen vacancy [51]. The XPS results are in good agreement with those obtained by CV further confirming the presence of Ti³⁺ species.

The binding energy and the percentage of Ti³⁺ and O2v species calculated by using the Multipack software are reported in Table 2. Although the percentage of Ti³⁺ slightly changes in all the samples, a linear correlation with the amount of O2v oxygen vacancies can be observed, as discussed later.

3.1.5. Structural analysis and other characterizations of the electrodes

The crystalline titania phases present in TiNT electrodes were characterized by glancing angle X-ray diffraction (GAXRD) measurements. The results were consistent with previous results and supported by high-resolution transmission electron microscopy [25] showing the presence of only TiO₂ anatase phase in samples annealed at 450 °C. On the other hand, reflections due to the TiO₂ rutile phase, in addition to those for the TiO₂ anatase phase, appear at an annealing temperature of 500 °C or higher (Fig. S7b in Supplementary Info). High-resolution transmission electron microscopy (HRTEM) characterization of the sample annealed at 450 °C [25] shows that the structure at the top is still characterized by a crystalline TiO₂ anatase structure, while the TiO₂ rutile phase is present at the bottom of the NTs, at the interface with the metallic Ti layer (Fig. S6 in Supplementary Info). The titania patches or debris at the surface of the TiO₂ NTs ordered array results instead amorphous.

For TiNT-HS (sample prepared by hydrothermal synthesis), following the calcination at 450 °C, well-defined lines for crystalline TiO₂ anatase are present (Fig. S7a in Supplementary Info).

Surface area measurements obtained by physical adsorption of N_2 on the samples at liquid nitrogen temperatures (Brunauer-Emmett-Teller (BET) method) indicate a surface area in the 50–60 m² g⁻¹ range for all TiNT samples (the N_2 isotherm measure at 77 K for the most representative sample, TiNT-T, was reported in Fig. S7c). In order to evaluate the Ti nanotubes surface area, some electrodes were prepared and the formed layer detached and used for BET analysis, thus it is representative for the Ti nanotubes surface area and not of the electrode itself.

3.2. Electrocatalytic performances in OX reduction

Fig. 5 shows the Faradic efficiencies (FE) to GO (glyoxylic acid, FE_{GO}) and GC (glycolic acid, FE_{GC}) and the OX (OX) conversion after 2 h of electrocatalytic tests at three applied potentials (-1.1, -1.2, and -1.3 V). All samples were tested with an OX concentration of 0.03 M. The experimental setup is shown in Fig S1(a) (Supplementary Info).

The electrocatalytic performances can be lumped into two groups:

- (i) TiNT and TiNT-A show low OX conversion (<10%) and predominant formation of GO with respect to GC, but lower cumulative FEs ($FE_{GO} + FE_{GC}$) in TiNT-A with respect to TiNT (the difference is in H_2 side formation).
- (ii) TiNT-T and TiNT-HS samples, showing about three times higher OX conversion with respect to the first group of electrodes, and also greater FE_{GC} with respect to FE_{GO} (with also higher global efficiency, FE_{GC} + FE_{GO} with respect to the first group of electrodes).

Performances are minorly affected by the variation in the applied potential tested, although the OX conversion slightly increases with it. The current density follows a similar trend except for the case of TiNT-A and TiNT samples where the difference, in terms of current density, is more affected by the applied potential. The current density profiles were reported in Fig. S7(d).

At the optimal applied potential of -1.1 V, the FE $_{GC}$ is equal to 58.3% and 60.8 % for TiNT-T and TiNT-HS, respectively.

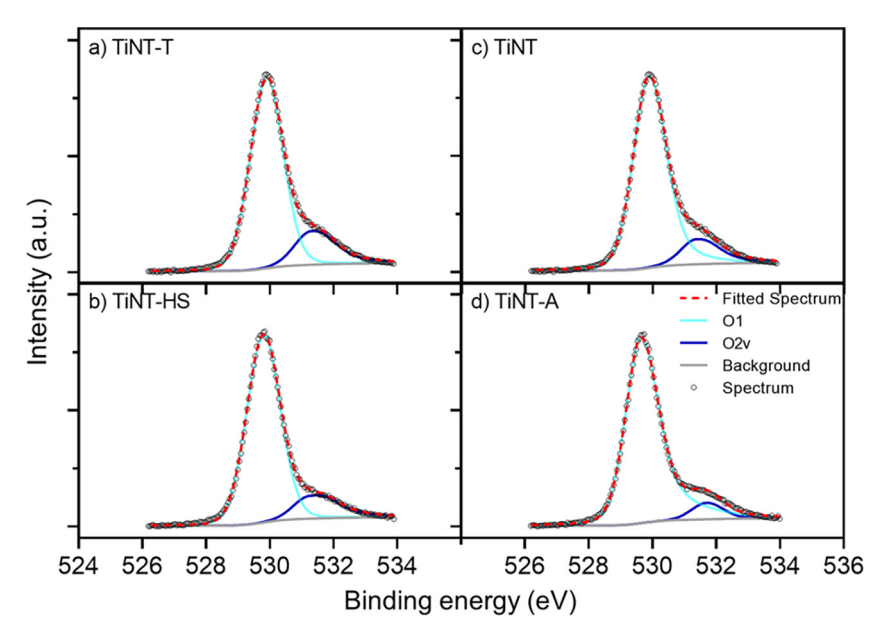
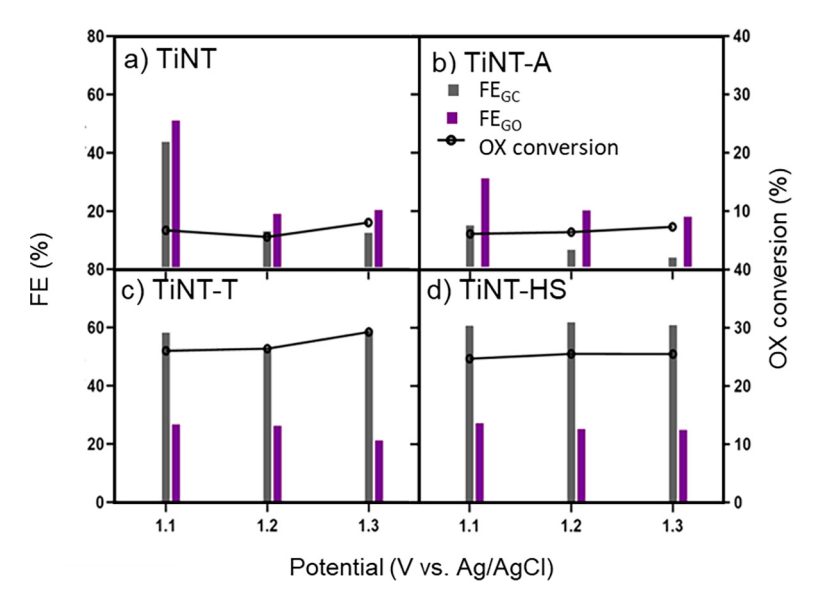


Fig. 4. O 1s photoemission spectra of the used electrodes.



 $\textbf{Fig. 5.} \ \ \text{Faradaic efficiency (FE) and conversion of OX at three potential investigated (-1.1; -1.2; -1.3) for the prepared electrodes.$

Table 2Binding energies (eV) of Ti 2p and O 1s peaks present in the XPS spectra of TiNT samples and the corresponding percentage of oxygen vacancies (O2v) and Ti³⁺.

	Ti ⁴⁺ (eV)		Ti ³⁺ (eV)		O (eV)	Compositi	on (%)				OX Conv _{avg} (%)
Sample	Ti 2p _{3/2}	Ti 2p _{1/2}	Ti 2p _{3/2}	Ti 2p _{1/2}	01	02v	0	Ti	02v	Ti ³⁺	_
TiNT	458.67	464.21	456.95	462.49	530.05	531.87	46.61	53.39	7.00	5.14	6.81
TiNT-A	458.45	463.99	456.88	462.42	529.64	531.70	47.21	52.79	6.80	5.11	6.62
TiNT-HS	458.50	464.04	456.91	462.45	529.81	531.32	45.94	54.06	14.70	5.54	26.00
TiNT-T	458.60	464.14	456.95	462.49	529.90	531.31	46.42	53.58	19.00	5.71	32.00

The OX conversion is similar for all the samples at each investigated potential, and the average value is reported in Table 2. It can be noted that the conversion increases from about 7% (for TiNT and TiNT-A) to 26% and 32%, respectively, for TiNT-HS and TiNT-T. The

complete set of electrocatalytic results (FE, conversion, Yield and average current density), including as comparison, also with the Ti foil after oxidative pretreatment at 450 °C (30 min) (Ti-T), i.e., the same pretreatment used for TiNT-T electrode before the anodic

oxidation, is reported in the Supplementary Info (Table S1). Not reported in Table S1 is the behavior of the Ti foil substrate, resulting fully inactive in GO or GC synthesis. After the pre-oxidation treatment (Ti-T), some activity is observed but largely inferior to the electrodes prepared by anodic oxidation due to the lower amount of nanostructured titania. These data confirm the role of TiO_2 as the electroactive element.

The removal of the surface ${\rm TiO_2}$ amorphous patches or debris by ultrasonic treatment, widely reported in literature in order to clean the electrode surface, [52,53] does not lead to performance improvements but rather to a minor or even negative effect (Fig. S8 in Supplementary Info) confirming their contribute on the electro reduction of OX.

All the elctrodes prepared were tested twice in order to have preliminary information about the stability. They showed only a sligtly lowering of the performances after 12 h of testing.

4. Discussion

4.1. Relationships between characteristics and reactivity of the electrodes

A series of linear relationships were observed between the features of the electrodes determined by the characterization methods discussed before and the electrocatalytic reactivity. The results are summarized in Fig. 6.

A linear correlation is present (Fig. 6b) between the intensities of the O2v peaks (attributed to oxygen vacancy) and the quantification of Ti3+ species by XPS analysis. Being TiO2 present in the form of NTs array, dense amorphous oxidic layer (TiNT-A), patches (TiNT) or debris (TiNT-T, TiNT-HS), while the ordered NTs array, not present in the TiNT-A sample (while in a different form in TiNT-HS), it may be concluded that the oxygen vacancies (O2v) are associated to the formation of reduced Ti ions (Ti3+) in amorphous TiO₂. Small debris interacting with the underlying TiO₂ NTs array, are easier reducible, and thus a higher amount of them is detected in TiNT-T, followed by TiNT-HS. More compact patches or debris result instead less reducible. This interpretation is well supported by the correlation observed between the anodic peak intensity obtained by CV (Fig. 3) and O2v concentration measured by XPS (Fig. 6c). The O2v concentration also linearly correlates with the average OX conversion (Fig. 6a). The reducibility of small oxide TiO₂ is thus the key to improving the reactivity in these electrodes.

Note, however, that the regression line does not pass through zero, but it intersects the X-axis at O2v = 7%, considering the anodic peak intensity between -0.8 and -0.9 V in CV tests (Ipa) vs. O2v correlation (see Fig. 6). The latter indicates that a small fraction of oxygen vacancies (O2v), is essentially inactive, possibly because located at the interface between the TiO_2 NTs and the Ti substrate, and thus largely inaccessible for the electrocatalytic activity.

In terms of GC synthesis, a nearly linear relationship could also be observed between the yield of GC ($Y_{\rm GC}$) with respect to the fraction of oxygen vacancies (O2v) (Fig. 7). The relationship is less accurate than those observed between O2v and Ti³+, OX conversion (OX Conv_{avg} reported in Table 2), and Ipa (Fig. 6). In addition, deviations from linearity are observed at lower applied potential, but where the average current densities are lower with a consequent higher estimated error, which is ±8% on the average. Nevertheless, the slightly less accurate relationship reported in Fig. 7 indicates reasonably that also the yield to GC (GO is the only other product of OX reduction detected, except minor traces of other products indicated in Scheme 1) well correlate to the same active species discussed in relation to the analysis of data in Fig. 6, e.g., small oxide TiO₂ nanoparticles.

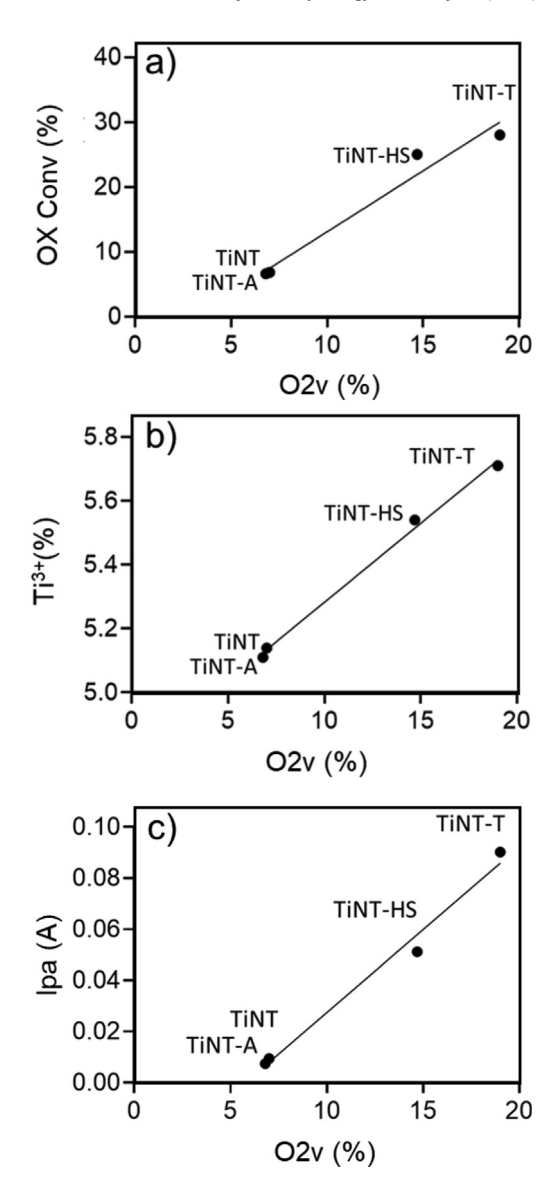


Fig. 6. Linear relationships observed in the series of TiNT electrodes between O2v (oxygen vacancies measured by XPS) percentage and (a) conversion of OX (OX), (b) concentration of Ti^{3^+} determined by XPS, and (c) an Ipa (peak intensity in CV tests for the anodic peak in the range between -0.8 V and -0.9 V).

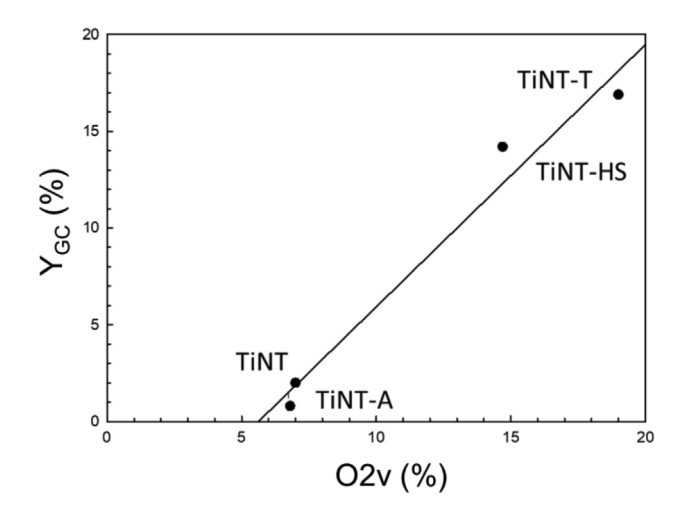


Fig. 7. Relationships observed in the series of TiNT electrodes between O2v (oxygen vacancies measured by XPS) percentage and yield of GC (Y_{GC} , %) for tests at -1.3 V.

4.2. Nature of the active species for the selective electroreduction of OX to GC

Discussion in the previous section, and relationships evidenced in Figs. 6(a) and 7 regarding OX conversion, yield of GC and concentration of oxygen vacancies (O2v), and related correlation with reducibility of the electrode (amount of Ti3+ by XPS and intensity of the anodic peak in CV experiments) evidence a clear correlation between reactivity and redox properties. By analyzing the different electrodes investigated, the data evidence that small oxide TiO₂ nanoparticles (small patches or debris) are responsible for the electrocatalytic behavior, due to their easy reducibility. However, the interaction with TiO2 NTs, stabilized following the calcination treatment, is also crucial to enhancing reducibility and avoiding sintering. Therefore, the active component is the hybrid system composed of TiO₂ nanotubes and small TiO₂ nanoparticles. Being in our experimental conditions, GO and GC are the only two products of OX reduction detected (other products are in small traces, and also side H₂ formation is not significant in the best samples), changing the nature of this interaction between TiO2 NTs and the supported TiO₂ (amorphous) nanoparticles also allow to tune the relative Faradaic selectivity to GC and GO.

A possible interpretation of these results is the following, although it is a tentative interpretation to offer a first mechanistic hypothesis rather than a proof. The nature of the reduced titania species formed can be tentatively explained by considering the crystalline plane (101) of the anatase phase, the most exposed on the surface, where an oxygen atom is bridging two Ti atoms, one with coordination number sixth and the other with coordination number five. Once this oxygen is removed, Ti changes its coordination number to 5 and 4, respectively, and the Ti⁴⁺ is reduced to Ti³⁺ by electron transfer in the 3d orbitals, obtaining a Ti₂O₃ like species. In TiO2, oxygen vacancies from the bulk or surface cause one or two free electrons. In this way, the place occupied by the O²⁻ anion in the lattice is taken by these free electrons in the defective crystal and the energetic cost of the vacancy formation is minimized [54]. These electrons have a direct effect on the electronic structure of TiO₂ by forming a donor level at 0.7 eV below the bottom conduction band [55]. It is reported that effects associated with oxygen vacancies can alter the adsorption of some small molecules like CO, N2O, H2O, H2O, H2OOH, promoting dissociative over molecular adsorption [54,56]. It is thus reasonable to expect that these oxygen vacancies also play a role in activating in a similar way also OX, thus leading to the enhanced activity.

4.3. Comparison with literature results

With respect to the earlier finding by Zhao et al. [18], using a roughened TiO₂ film electrode, apart from the lower applied voltages necessary in our case (2.9-3.4 V were used by Zhao et al. [18] possibly for the low conductivity of their electrodes, as confirmed from the long reaction times they used), we observed GC as the main product (in the best sample, TiNT-T) rather than GO, moreover a correlation between OX conversion and selectivity to GC was demonstrated. On the other hand, GO is intermediate to GC (Scheme 1), and thus it is well rational that an electrode with very low activity is necessary to stop to this intermediate. While GO is a product with higher added value than GC (around twice), electrode activity is equally crucial for the industrial development of this route. From the practical perspective, data presented here show that two classes of electrodes prepared by anodic oxidation could be indicated. TiNT-T, where a pre-calcination step of Ti starting foil is made, giving higher OX conversion and GC yield, and a "conventional" preparation by anodic oxidation (TiNT), showing lower activity (but still acceptable) and coproducing GO and GC in similar amounts, but with a slight prevalence of the former. Thus, changing the electrode makes it possible to have a process where the GC to GO ratio is changed depending on market requests.

These results agree with those recently obtained by Yamamuchi et al. [57], who studied Ti-Zr oxide particles as electrodes for GC synthesis by OX electrocatalytic reduction, not using a full electrocatalytic cell, but rather CV and chronoamperometry tests at 50 °C. They conclude that amorphous rather than crystalline oxide is required in order to obtain better electrocatalytic performances. Atomic disordering would likely stabilize the formation of oxygen vacancies and reducibility of the oxide, although characterization data on these aspects were not provided. Yamamuchi et al. [57] also showed that the less active samples show enhanced GO formation, while GC was maximized in the most active ones. Due to differences in the experimental campaign, a direct comparison of the data is not possible, but their results obtained with Ti-ZrO₂ particles are well in line with those presented in Fig. 5.

The same research group [58] also investigated the light-assisted electrochemical OX reduction (in the presence of external bias) using a TiO₂ cathode and a WO₃ photoanode, obtaining 80% of FEs (FE_{GC} + FE_{GO}) applying a potential of 1.5 V vs. reversible hydrogen electrode (RHE) under ultraviolet (UV)-visible irradiation (λ > 300 nm) at 50 °C for 2 h. The cathode was prepared by depositing TiO₂ nanoparticles over a Ti foil, but the robustness of these electrodes is weak, and as indicated by authors also reaction rates were low (few μ mol h^{-1}), around two–three orders of magnitude lower than those we observed.

Recently Yang et al. [59], using multi-walled carbon nanotubes (MWNT) wrapped by an anatase ${\rm TiO_2}$ layer, reported an OX conversion and GC selectivity of 51.2% and 38.7%, respectively at an applied potential of -2.2 V vs. RHE and 60 °C. The maximum reported yield in GC is thus around 19%, well in line with that we reported (Fig. 7), but at room temperature rather than 60 °C and not using an expensive anode electrode (IrO₂) as used by them. In addition, they did not report the formation of GO, considering that GC is the dominant product and its Faradaic selectivity is only about 40%, which indicates a significant formation of ${\rm H_2}$ as a side product.

Sadakiyo et al. [60] developed a PEAEC (polymer electrolyte alcohol electrosynthesis cell) containing porous ${\rm TiO_2}$ obtained by hydrothermal synthesis, on a Ti felt as a cathode, obtaining nearly complete OX conversion and 31.9% ${\rm FE_{GC}}$ at 3.0 V applied voltage at 60 °C. However, the maximum energy conversion efficiency was less than 50%. Furthermore, the dominant product in terms of FE in these conditions was ${\rm H_2}$, with FE around 60%. Specific current density to GC is about 20 mA cm⁻² which compares well with around 10 mA cm⁻² values we obtained but at room temperature and application of a lower potential. In addition, Sadakiyo et al. [60] results show a lowering of the current density in already 2 h of tests.

Because of the different conditions reported in literature and incomplete information about the FE, GC selectivity/yields, it is quite difficult to summarize all the relevant data for a fair comparison. Anyway, focusing on the energetic features, the literature results are obtained at higher potentials, and thus with greater energy consumption. The present work demonstrated the possibility of a green synthetic process for the production of an alcoholic compound from an organic acid assisted by water electrolysis at the low potential of -1.1 V vs. Ag/AgCl (-0.78 vs. RHE) and room temperature by using hybrid electrodes based on TiOx debrits/ TiO₂ NTs array supported on Ti foils.

5. Conclusions

The analysis of the characteristics and reactivity of a series of electrodes prepared by anodic oxidation of Ti foils provide indications about the nature of the active species for the electrocatalytic reduction of OX to glycolic acid. These electrodes are robust and less toxic with respect to lead electrodes mostly studied in this reaction. They can also be prepared with low-cost procedures which can be scaled up. They do not need high potentials to operate efficiently, and the compared with literature results demonstrates the possibility of a green, renewable energy-driven process for the production of an alcoholic compound from an organic acid at the low potential of -1.1~V~vs.~Ag/AgCl~(-0.78~vs.~RHE) at room temperature, not using critical raw materials and expensive or toxic electrodes. Coupled with an electrochemical synthesis of the OX from CO₂, the process represents a new green and low-carbon path to produce added value chemicals from CO₂.

The electrodes investigated have different characteristics. TiNT-A shows the presence of a dense nanostructured TiO₂ layer without the presence of TiO₂ nanotubes. TiNT and TiNT-T, and TiNT-HS used as alternative preparation leading to nanotubes also without an ordered packing, show the presence of small amorphous patches, debris, or TiO₂ nanoparticles together with the TiO₂ nanotubes. They differ in terms of the characteristics of these amorphous TiO₂ nanoparticles, and the differences could be related to the details of the preparation procedure, with the anodization curves (Fig. 1) providing good indications about the formation mechanism.

A series of relationships between the characteristics of these samples, in particular, the concentration of oxygen vacancies (O2v) and the amount of Ti^{3+} detected in XPS or the intensity of the anodic peak in CV tests, and the catalytic behavior (OX conversion and yield of GC, Y_{GC}) evidence the relation between these aspects. The analysis of the results indicates that the small amorphous TiO_2 nanoparticles (or surface patches or debris) intercating with TiO_2 NTs, represent the sites responsible for the conversion of OX and GC yield. By varying this structural characteristic of the electrodes, it is possible to tune the GC to GO relative ratio.

Declaration of Competing Interest

The authors declare that they have no known competing financial interests or personal relationships that could have appeared to influence the work reported in this paper.

Acknowledgments

This project has received funding from the European Union's Horizon 2020 research and innovation program under grant agreement ID 767798 (OCEAN). This MIUR PRIN 2017 project CO2 ONLY project nr. 2017WR2LRS gratefully acknowledged.

Appendix A. Supplementary data

Supplementary data to this article can be found online at https://doi.org/10.1016/j.jechem.2021.12.034.

References

- [1] A. Mustafa, B.G. Lougou, Y. Shuai, Z. Wang, H. Tan, J. Energy Chem. 49 (2020) 96–123.
- [2] D. Saygin, D. Gielen, Energies 14 (2021) 3772.
- [3] R.S. Norhasyima, T.M.I. Mahlia, J. CO₂ Utiliz. 26 (2018) 323–335.
- [4] P. Lanzafame, S. Abate, C. Ampelli, C. Genovese, R. Passalacqua, G. Centi, S. Perathoner, ChemSusChem 10 (2017) 4409–4419.
- [5] S. Perathoner, G. Centi, Catal. Today 330 (2019) 157-170.
- [6] J. Huang, T. Yang, K. Zhao, S. Chen, Q. Huang, Y. Han, J. Energy Chem. 62 (2021) 71–102.
- [7] W. Zhu, K. Zhao, S. Liu, M. Liu, F. Peng, P. An, B. Qin, H. Zhou, H. Li, Z. He, J. Energy Chem. 37 (2019) 176–182.

- [8] Y. Zheng, A. Vasileff, X. Zhou, Y. Jiao, M. Jaroniec, S.-Z. Qiao, J. Am. Chem. Soc. 141 (2019) 7646–7659.
- [9] L. Fan, C. Xia, F. Yang, J. Wang, H. Wang, Y. Lu, Sci. Adv. 6 (2020) eaay3111.
- [10] E. Boutin, M. Robert, Trends Chem. 3 (2021) 5.
- [11] M.A. Murcia Valderrama, R.J. van Putten, G.J.M. Gruter, Eur. Polym. J. 119 (2019) 445–468.
- [12] J. Iglesias, I. Martínez-Salazar, P. Maireles-Torres, D. Martin Alonso, R. Mariscal, M. López Granados, Chem. Soc. Rev. 49 (2020) 5704–5771.
- [13] A.C. Garcia, C. Sanchez-Martinez, I. Bakker, E. Goetheer, ACS Sustainable Chem. Eng. 8 (2020) 10454–10460.
- [14] J.R. Ochoa, A. de Diego, J. Santa-Olalla, J. Appl. Electrochem. 23 (1993) 905–909.
- [15] Y.L. Zhou, X.S. Zhang, Y.C. Dai, W.K. Yuan, Chem. Eng. Sci. 58 (2003) 1021– 1027.
- [16] J. Li, X. Hu, Y. Su, Q. Li, Chem. Eng. Sci. 62 (2007) 6784-6793.
- [17] S. Masaaki, H. Shinichi, C. Xuedong, Y. Miho, S. Masaaki, Y. Miho, Sci. Rep. 7 (2017) 17032.
- [18] F. Zhao, F. Yan, Y. Qian, Y. Xu, C. Ma, J. Electroanal. Chem. 698 (2013) 31-38.
- [19] F. De Luca, R. Passalacqua, F.P. Abramo, S. Perathoner, G. Centi, S. Abate, Chem. Eng. Trans. 84 (2021) 37–42.
- [20] X. Nie, S. Yin, W. Duan, Z. Zhao, L. Li, Z. Zhang, Nano 16 (2021) 2130002.
- [21] Q. Zhou, Z. Fang, J. Li, M. Wang, Microporous Mesoporous Mater. 202 (2015)
- [22] K. Lee, A. Mazare, P. Schmuki, Chem. Rev. 114 (2014) 9385-9454.
- [23] C.A. Grimes, J. Mater. Chem. 17 (2007) 1451-1457.
- 24] G. Centi, S. Perathoner, Eur. J. Inorg. Chem. 26 (2009) 3851–3878.
- [25] R. Passalacqua, S. Perathoner, G. Centi, Catal. Today 251 (2015) 121-131.
- [26] G. Centi, S. Perathoner, Coord. Chem. Rev. 255 (2011) 1480-1498.
- [27] C. Ampelli, R. Passalacqua, S. Perathoner, G. Centi, D.S. Su, G. Weinberg, Topics Catal. 50 (2008) 133-144.
- [28] R. Passalacqua, C. Ampelli, S. Perathoner, G. Centi, Nanosci. Nanotechn. Lett. 4 (2012) 142–148.
- [29] G. Centi, R. Passalacqua, S. Perathoner, Mater. Sci. Semiconductor Proc. 42 (2016) 115–121.
- [30] K.C. Sun, M.B. Qadirm, S.H. Jeong, RSC Adv. 4 (2014) 23223-23230.
- [31] A. Nakahira, T. Kubo, C. Numako, Inorg. Chem. 49 (2010) 5845-5852.
- [32] S. Du, Engineering 7 (2021) 33-49.
- [33] M.Z.H. Khan, X. Liu, J. Electronic Mater. 48 (2019) 4148-4165.
- [34] M. Madian, A. Eychmueller, L. Giebeler, Batteries, 4 (2018) 7/1-36.
- [35] Y. Zhang, Y. Tang, W. Li, X. Chen, ChemNanoMat 2 (2016) 764-775.
- [36] T. Berger, D. Monllor-Satoca, M. Jankulovska, T. Lana-Villarreal, R. Gomez, ChemPhysChem 13 (2012) 2824–2875.
- [37] G. Centi, R. Passalacqua, S. Perathoner, D.S. Su, G. Weinberg, R. Schlögl, Phys. Chem. Chem. Phys. 9 (2007) 4930–4938.
- [38] A. Apolinário, P. Quitério, C.T. Sousa, J. Ventura, J.B. Sousa, L. Andrade, A.M. Mendes, J.P. Araújo, J. Phys. Chem. Lett. 6 (2015) 845–851.
- [39] P. Roy, S. Berger, P. Schmuki, Angew. Chemie Int. Ed. 50 (2011) 2904-2939.
- 40] S.P. Albu, P. Roy, S. Virtanen, P. Schmuki, Isr. J. Chem. 50 (2010) 453–467.
- [41] J.M. Macak, S.P. Albu, P. Schmuki, Phys. Status Solidi Rapid Res. Lett. 1 (2007) 181–183.
- [42] M. Moazeni, H. Hajipour, M. Askari, M. Nusheh, Mater. Res. Bull. 61 (2015) 70-75.
- [43] V.A. Sugiawati, F. Vacandio, A. Galeyeva, A.P. Kurbatov, T. Djenizian, Front. Phys. 7 (2019) 179.
- [44] F. Fabregat-Santiago, I. Mora-Seró, G. Garcia-Belmonte, J. Bisquert, J. Phys. Chem. B 107 (2003) 758–768.
- [45] H. Yu, J. Ma, Y. Zhang, X. Zhang, W. Shi, Electrochimica Acta 56 (2011) 6498–6502.
- [46] N. Makivić, J.-Y. Cho, K.D. Harris, J.-M. Tarascon, B. Limoges, V. Balland, Chem. Mater. 33 (2021) 3436–3448.
- [47] S. Bellamkonda, N. Thangavel, H.Y. Hafeez, B. Neppolian, G. Ranga Rao, Catal. Today 321–322 (2019) 120–127.
- [48] T. Gakhar, A. Hazra, Nanoscale 12 (2020) 9082-9093.
- [49] Z. Li, H. Bian, X. Xiao, J. Shen, C.O. Zhao, J. Lu, Y. Li, ACS Appl. Nano Mater. 2 (2019) 7372–7378.
- [50] B. Bharti, S. Kumar, H.N. Lee, R. Kumar, Sci. Rep. 6 (2016) 1–12.
- [51] X. Zhang, H. Tian, X. Wang, G. Xue, Z. Tian, J. Zhang, S. Yuan, T. Yu, Z. Zou, Mater. Lett. 100 (2013) 51–53.
- [52] H. Xua, Q. Zhang, C. Zheng, W. Yan, W. Chu, Appl. Surface Sci. 257 (2011) 8478–8480
- [53] W.A. Abbas, I.H. Abdullah, B.A. Ali, N. Ahmed, A.M. Mohamed, M.Y. Rezk, N. Ismail, M.A. Mohamed, N.K. Allam, Nanoscale Adv. 1 (2019) 2801–2816.
- [54] X. Pan, M.Q. Yang, X. Fu, N. Zhang, Y.J. Xu, Nanoscale 5 (2013) 3601–3614.
- [55] C. Di Valentin, G. Pacchioni, A. Selloni, J. Phys. Chem. C 113 (2009) 20543– 20552.
- [56] D.N. Pei, L. Gong, A.Y. Zhang, X. Zhang, J.-J. Chen, Y. Mu, H.Q. Yu, Nat. Commun. 6 (2015) 2–11.
- [57] M. Yamauchi, S. Hata, H. Eguchi, S. Kitano, T. Fukushima, M. Higashi, M. Sadakiyo, K. Kato, Catal. Sci. Technol. 9 (2019) 6561–6565.
- [58] S. Kitano, M. Yamauchi, S. Hata, R. Watanabe, M. Sadakiyo, Green Chem. 18 (2016) 3700–3706.
- [59] J. Yang, J. Cheng, J. Tao, M. Higashi, M. Yamauchi, N. Nakashima, ACS Appl. Nano Mater. 2 (2019) 6360–6367.
- [60] M. Sadakiyo, S. Hata, X. Cui, M. Yamauchi, Sci. Rep. 7 (2017) 1-9.